Long-term spatio-temporal changes of wetlands in Tibetan Plateau and their response to climate change

Yang Li [a,1], Zhengyang Hou [a,1], Liqiang Zhang [a,*], Ying Qu [a], Guoqing Zhou [c], Jintai Lin [b], Jingwen Li [c], Ke Huang [a]

[a] State Key Laboratory of Remote Sensing Science, Faculty of Geographical Science, Beijing Normal University, Beijing 100875, China
[b] Laboratory for Climate and Ocean-Atmosphere Studies, Department of Atmospheric and Oceanic Sciences, School of Physics, Peking University, Beijing 100871, China
[c] College of Geomatics and Geoinformation, Guilin University of Technology, Guilin 541004, China

ARTICLE INFO

ABSTRACT

Understanding the changes of wetlands on the Tibetan Plateau (TP) is important for action to ensure ecosystem resilience in Asia. However, mapping long-term changes of wetlands at high resolutions remains challenging. Here, we quantify the spatio-temporal changes of TP wetlands from 1990 to 2019, by combining Landsat imagery with deep learning to map TP wetlands. The deep learning model combined with transfer learning strategies achieves high classification performance using a few class samples. The validation results show that the user's accuracy is 95.5% and the producer's accuracy is 90.1% for wetland extraction, satisfying with subsequent analysis of wetland spatio-temporal changes. Based on the wetland extraction model, we have created annual wetland map in the TP for the first time. We find that the areal extent of TP wetlands has increased by 31.2 ± 6.6 % over the past 30 years. The growth is particularly noticeable (by 22.5 ± 6.2 %) during 2015–2019. Spatially, the wetland areal extent on the Qiangtang Plateau (in the inner part of TP and as habitats of various birds and rare wild animals) and the source region of Yangtze River show the largest expansions by 55.3 ± 9.3 % and 44.0 ± 8.9 %, respectively. Such rapid wetland expansions are associated with increasing rainfall and temperature which have heterogeneous influences on wetland changes across the TP. Our findings provide evidence for the impact of climate change on wetland area. The marked wetland changes highlight that climate mitigation is a priority for high-latitude ecosystems.

1. Introduction

Wetlands are critical to human survival and development as one of the three major ecosystems (Chatterjee et al., 2015). They provide essential biodiversity and ecosystem services, which are crucial to hydrology, biogeochemical function, and biodiversity conservation (Cohen et al., 2021; Gall et al., 2013; Xi et al., 2020; Russi et al., 2013). Wetlands are the largest component of the terrestrial biological carbon pool for sequestering and storing carbon from the atmosphere (Chmura et al., 2003; Mitsch et al., 2013). Moreover, wetlands are also the world's largest natural source of methane (CH_4), accounting for one third of total natural and anthropogenic emissions (Hu et al., 2014; Tian et al., 2016; Zhang et al., 2017). Global wetlands have been experiencing remarkable shrinking during the recent decades due to intensive human activities and climate change (Creed et al., 2017; Davidson, 2014).

The Tibetan Plateau (TP), known as the "Third Pole" of the Earth and "Asian Water Tower", is the magnifier of global climate change and the birthplace of many large rivers in Asia. There are unique alpine wetlands on the TP, accounting for 20% of the wetlands area in China, and the lakes alone constitute half of the national lake area (Zhao et al., 2015). These alpine wetlands have been less influenced by direct human disturbances, but more sensitive to climate variability (Arneth et al., 2010). Climate variability has imposed large environmental impacts on the TP in the past three decades (Wang et al., 2020a). However, measuring the long-term dynamics of wetlands remains a challenge due to the uncertainty of wetland boundaries, the complexity of spectral and texture characteristics (Feng et al., 2019) as well as the lack of the wetland class samples on the TP.

As a result, the spatio-temporal variations of TP wetlands and their linkage to climate variability remain little known. Previous maps and datasets on the TP wetlands are generated at intervals of 5 years or more (Gong et al., 2010; Niu et al., 2012) or at coarse spatial resolutions (e.g.,

1 km) (Hu et al., 2017). Such coarse resolutions and time incompleteness cannot capture the complexities of spatio-temporal dynamics of wetlands as well as how climate affects wetland changes. Mapping long-term changes in wetland occurrence, documenting multi-decadal trends and identifying the timing of wetland expansion and retreat are important to provide insight into the impacts of climate change and climate variability on wetland distribution. Therefore, there is an urgent need to develop annual maps of TP wetlands at a high spatial resolution over the past decades that can be used to explore the changes and drivers of TP wetlands.

Deep convolutional neural networks (CNNs) have shown impressive performance and are rapidly being used in large numbers within the field of remote sensing image classification. However, deep learning models contain a vast number of trainable parameters and require a large number of labeled datasets to achieve high performance. Those annotations are time-consuming and require expert knowledge or on-the-ground surveys. The lack of annotations limits their performance in many methods of supervised learning (Ayush et al., 2021; Mañas et al., 2021). On the other hand, it has been found that deep learning methods are robust to noise in the training labels (Kaiser et al., 2017). The study by Sun et al. demonstrated that the scale of data can overpower noise in the label space and increasing the number of training samples can improve model performance (Sun et al., 2017). Some work has explored the application of transfer learning to address the lack of annotations. Kaiser et al. showed that training a CNN using large-scale, highly noisy labels from OpenStreetMap of other cities can provide an accurate segmentation of buildings and streets in a city (Kaiser et al., 2017). Kemker et al. demonstrated that pre-training a CNN using synthetic aerial images and then fine-tuning it with real data can significantly improve segmentation performance (Kemker et al., 2018). This makes it possible to avoid annotating large amounts of training data and instead train the classifier from existing legacy data, even though these data may exhibit high levels of noise.

Here, we present a novel deep learning-based scene classification framework to extract wetlands from the Landsat 5, 7 and 8 images spanning the past 30 years. With the supervised learning in scene classification, our model can better carry a semantic-level understanding of the meanings and contents of images(Wang et al., 2015; Wei et al., 2022). Through automatic wetland recognition and extraction, for the first time, we create annual maps of TP wetlands at 30 m spatial resolution from 1990 to 2019. We find that the TP wetland areal extent has experienced a rapid increase of 31.2 ± 6.6 over the past 30 years. Based on our analysis of annual wetland and climate data, we find that the rapid wetland expansion is associated with increasing rainfall and rising temperature which have heterogeneous influences on wetland changes across the TP. Our findings serve as a foundation for accurately characterizing the changes on wetlands in the TP and the response to climate change.

2. Datasets

2.1. Landsat images

Landsat images are taken from the United States Geological Survey website (https://www.usgs.gov/), including Landsat 5 Thematic Mapper (TM) for the 1990 s, Landsat 7 Enhanced Thematic Mapper Plus (ETM +) from 2000 to 2012, and Landsat 8 OLI sensor from 2013 to 2019. Altogether, 137 scenes of Landsat images with paths from 130 to 151 and rows from 32 to 42 are needed to cover the entire land area of TP (Fig. 1a). Most of the images are obtained between September and October per year (Fig. 1b), assuring that they have similar environmental and hydrological conditions. For the images with the cloud cover of over 6%, we utilized the quality assurance (QA) band to identify the clouds or cloud shadows and downloaded the second image to replace the cloud-covered regions. If the images between September and October are not enough to synthesize cloud-free images, we choose the images from the neighboring months. Finally, a total of 6,050 Landsat images are captured for wetland extraction. We use the inverse distance
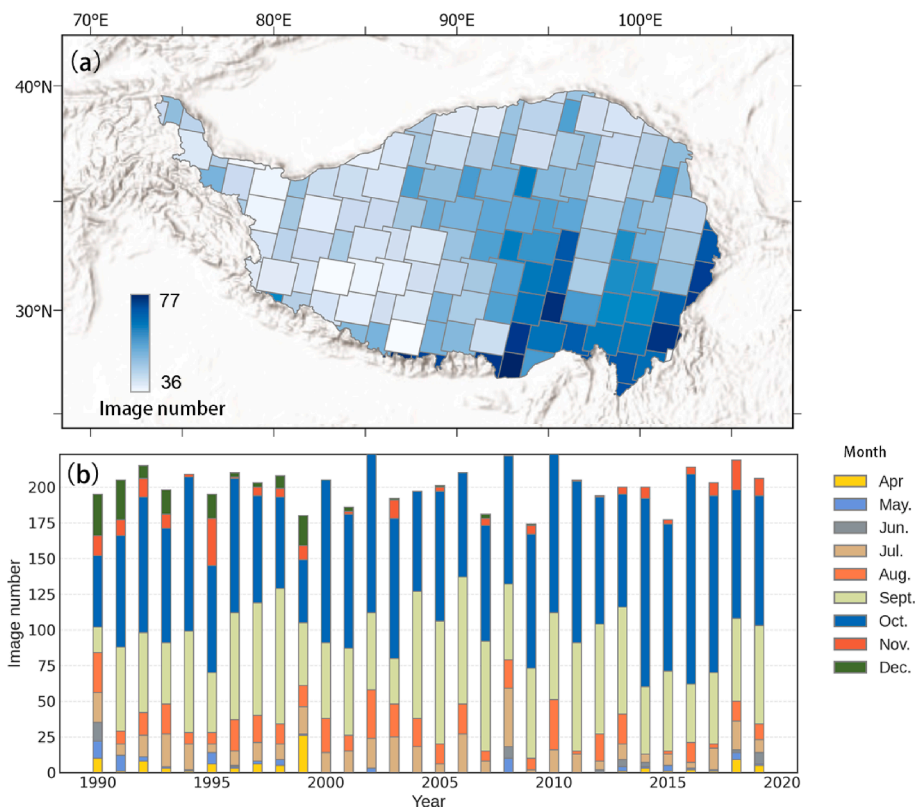

Fig. 1. Landsat image acquisition covering the TP. (a) The number of Landsat images for each grid (Path/row) in 30 years; (b) The months for capturing images.

weight interpolation algorithm to fill the gaps in the images of the Landsat 7 ETM + sensor after 2003 (Chen et al., 2011).

All images undergo geometric, terrain and radiation corrections to obtain the top-of-atmosphere (TOA) reflectance data. Six common bands of the three Landsat sensors, i.e. Band1-Band5 and Band7 for TM and ETM sensors, and Band2-Band7 for OLI sensors, are used to classify wetlands. Furthermore, The normalized difference vegetation index (NDVI) and the modified normalized difference water index (mNDWI) are used to acquire information on the water surface and vegetation-covered areas (Huang et al., 2014). Adding these data to the deep-learning model can speed up the convergence of the model.

2.2 Digital elevation model (DEM) data

Since optical sensors cannot penetrate clouds and vegetation cover, there are limitations in extracting wetlands by multispectral optical images alone (Guo et al., 2017; Zhou et al., 2017). Most wetlands are lowlands surrounded by uplands, which means that the classifiers can provide more accurate results if supported by ancillary data such as Digital Elevation Models (DEMs) (Hogg and Todd, 2007). We use DEM data with a resolution of 30 m from the Space Shuttle Radar Terrain Mission (SRTM). Google Earth Engine (GEE) cloud processing platform are used to collect the elevation of TP and calculate the slope of the terrain surface. The DEM images with 2 bands are stacked with the annual Landsat images and fed into the deep learning model for wetland extraction.

2.3 Climate data

Climate change affects the hydrology of wetland ecosystems mostly through changes in precipitation and temperature with great global variability. Other variables related to climate, such as evaporation, play important roles in determining regional and local impacts (Erwin, 2008). We used surface air temperature, precipitation, and potential evaporation as measures of regional climate in TP. Temperature and precipitation data are derived from the daily meteorological dataset of China National Surface Weather Station (V3.0) which contains quality-controlled daily values of temperature and precipitation for 84 meteorological stations across the TP. We compute the annual average temperature and precipitation for each region in TP from 1990 to 2019. Evaporation data are obtained from the Global Land Evaporation Amsterdam Model (https://www.gleam.eu) based on the data from weather stations and remote sensing data (Martens et al., 2017).

3. Methodology

As shown in Fig. 2, we trained a deep learning model based on scene classification to extract wetlands. The process mainly consists of five steps, i.e. data pre-processing, generation of training samples, model training, wetland boundaries segmentation and accuracy assessment. The trained model is used to identify wetlands from the satellite images from 1990 to 2020. Finally, we investigated the relationship between wetland area change and climate variation.

3.1 The definition of wetlands and our focused categories

Wetlands defined by the Ramsar Convention cover a range of natural and artificial areas like marshes, fens, peatlands, and bodies of water. These areas may contain static or flowing water. Considering that wetlands such as constructed wetlands, forest swamps and coastal wetlands, are very few in the TP (Gong et al., 2010), we focus on the following categories of wetlands in the TP, namely, lakes and lake wetlands
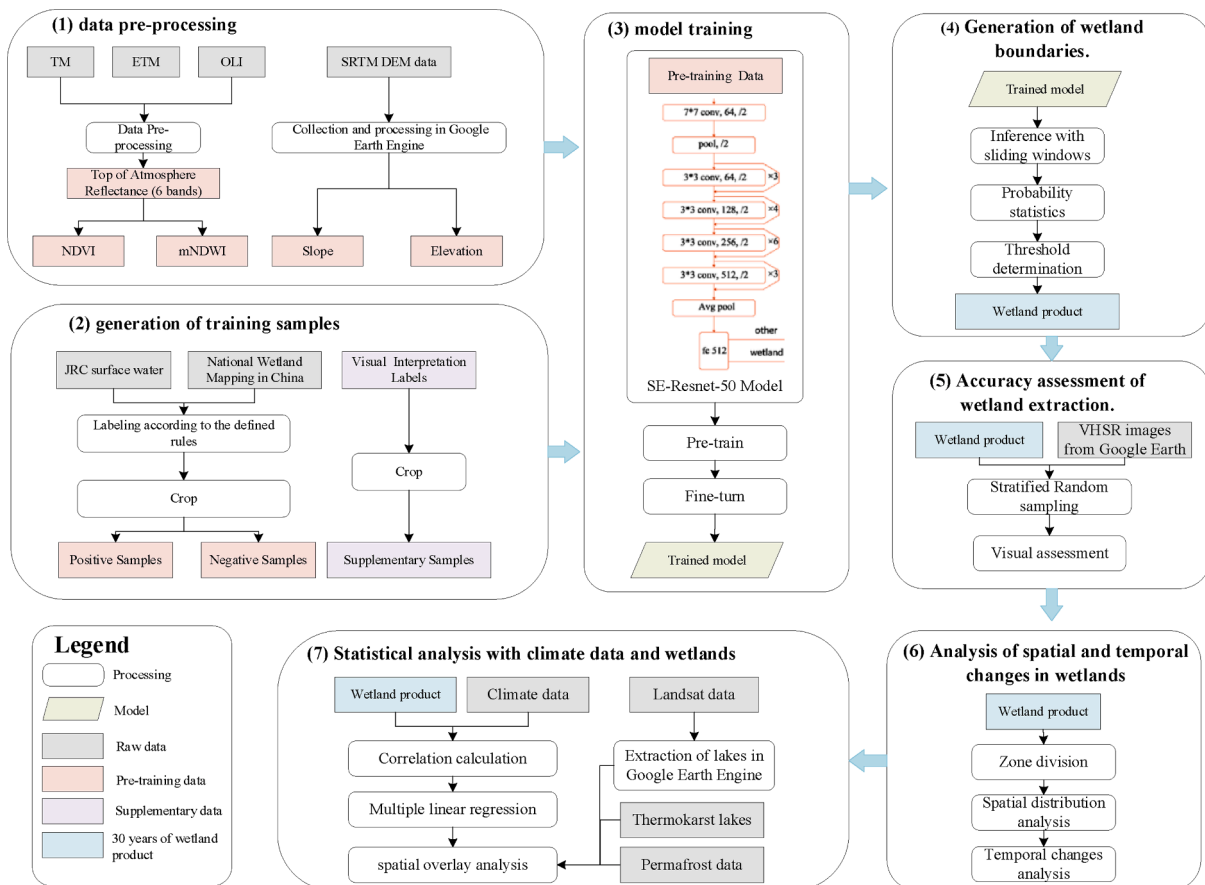

Fig. 2. The framework of our study.

including lake beaches, salt lakes; rivers and river wetlands including river beaches; and vegetated wetlands consisting of moss marshes, herbaceous marshes and salt marshes.

3.2 Generation of training samples

The training samples are derived from two data sources. The first one used for the pre-training is generated from JRC surface water data (Pekel et al., 2016) and the Chinses national wetland data (CAS_Wetlands) (Mao et al., 2020). The second source came from the manually annotated data with the help of very high spatial resolution (VHSR) images from Google Earth and the available wetland products like FROM-GLC (https://data.ess.tsinghua.edu.cn/), CAS_Wetlands (https://www.geodata.cn) and Global Land Cover at a 30 m resolution (GLC_FCS30, https://data.casearth.cn). >20,000 km^2 of the wetlands are annotated through visual interpretation to generate wetlands samples for fine-tuning the model.

The positive samples (wetland samples) are created as follows. The JRC surface water data and manually labeled data are taken as the reference data to create positive samples (wetland samples). The reference images are aligned with Landsat images, and then the two types of data (reference images and Landsat images) are cropped into image patches with 50 × 50 pixels, respectively. If the areal percentage of the wetland (or surface water) in each reference image patch exceeds 60%, the corresponding Landsat image patch is labeled as wetland. For a patch where riverine wetlands are distributed, the percentage of surface water is often<60%. Therefore, if there are riverine wetlands passing through the reference image patch, the corresponding Landsat image patch is also labeled as wetland. Finally, we generate 428,182 samples from JRC surface water data and 34,232 samples from manually labeled images.

The process for creating non-wetland samples is similar to that of positive samples. The CAS_Wetlands data are aligned with Landsat images, and then the two datasets are also cropped into 50 × 50 pixels image patches. If the percentage of wetland is 0 in a CAS_Wetlands image patch, the corresponding image patch is labeled as a non-wetland sample. Due to a large number of non-wetland samples, we randomly select one-tenth of them to balance the positive and negative samples.

3.3 Training of the deep learning model

The data used to train the deep learning model are 50 × 50 pixels image patches including ten bands, i.e. the six original bands from Landsat imagery, NDVI band, mNDWI band, elevation band and slope band. The data are fed into the deep learning model constructed based on SE-Resnet-50 (Hu et al., 2018). We modify the first layer of the network so that it can accept multi-modality images.

The pre-training data consist of 779,406 image patches, including 428,182 wetland samples and 351,224 non-wetland samples. 10% of the image patches are randomly selected as validation. The network is pre-trained using stochastic gradient descent (SGD) with 256 images as a mini-batch and a learning rate of 0.001. The momentum is set to 0.9, and the weight decay is 10^{-4}. The training stops until the average accuracy on the validation dataset stopped improving and remained stable, which took about 50 epochs. We combine 34,232 manual annotations of wetland samples and the same number of non-wetland samples for fine-tuning the pre-trained model. We adjust the learning rate to 0.0005. Other hyperparameters of the model are set the same as these of the pre-training, with a total of 40 epochs for fine-tuning.

3.4 Generation of wetland boundaries

The wetland objects extracted from Landsat images using the above scene classification strategy often contain some non-wetland pixels. Considering a wetland object is usually a region on the image, we exclude the non-wetland pixels and obtain the accurate boundary of the wetland by a sliding window. For each Landsat image, we crop the image patch by the sliding window and feed it into the trained deep learning model. The window size is 50 pixels, and the sliding step is 5, so each pixel in the Landsat image is tested 100 times. The pixels near the image margin are filled with zero so that they are also tested 100 times. We sum over all the results to obtain the final probability to determine whether the pixel is on a wetland object. The wetland boundary determination is sensitive to the final probability value. Therefore, a total of 1000 points are stratified randomly selected to verify the effect of different probability values as thresholds on the accuracy of the generated wetland boundaries.

The threshold represents the minimum times that a pixel is classified as a wetland in different scenes. For the threshold of which value ranges from 70 to 100, about 33 points are randomly selected to validate their classification accuracy (F1 value). As the threshold increases, the accuracy of wetland classification increases while the recall decreases. The final threshold is determined according to the maximum of the F1 values. With a threshold of 85, the recall curve and accuracy curve have an intersection where the F1 value reaches its highest (Fig. 3) at 94.2. We finally set 85 as the threshold for wetland mapping.

3.5 Accuracy assessment of wetland extraction

The stratified random sampling method combined with VHSR images is a widely used validation approach for accuracy assessment of land cover classification (Stehman and Foody, 2019; Wang et al., 2020b). 688 wetland samples and 5,682 non-wetland point samples from 1990 to 2019 are randomly selected for validating the performance of our method. Each sample has been interpreted independently by two individuals with the help of the VHSR images and multi-temporal Landsat images.

Three metrics were used to validate wetland mapping accuracy: user's accuracy (UA), producer's accuracy (PA), and F1 score. UA quantifies the proportion of the target class that agrees with the visual interpretation results, which measures commission error, or classification precision. PA quantifies the probability that the target class correctly classified by the wetland map, measuring omission errors. F1 score is the harmonic mean of precision and recall for each category (Bargiel, 2017).

The standard error of the error-adjusted estimated areas with the approximate 95% CI is used to quantify the uncertainty of the wetland areal extent (Stehman and Foody, 2019):

$$\widehat{A}_j \pm 1.96 \times S(\widehat{A}_j)$$

$$S(\widehat{A}_j) = A_{tot} \times \sqrt{\sum_{i=1}^{2} W_j^2 \frac{\frac{n_{ij}}{n_{i.}}\left(1 - \frac{n_{ij}}{n_{i.}}\right)}{n_{i.} - 1}}$$

where the total area of the TP is A_{tot}, the mapped area of the wetland is $\widehat{A_j}$, and $W_j = \widehat{A_j}/A_{tot}$. n_{ij} is the elements of the i-th row and j-th column, and $n_{i.}$ is the sum of the i-th row in the error matrix of the samples.

3.6. Statistical analysis

Initially, the correlation coefficients between the wetland area and the annual mean surface air temperature (AT), annual precipitation (AP), and annual potential evapotranspiration (APE) are calculated across the TP. Next, we use a multiple linear regression model (MLM) to establish the relationship between wetland area change and multiple climate variables. Finally, to explore the mechanisms of climate change impacts on wetland areas, we employ spatial overlay analysis to investigate the relationship between permafrost and wetlands.
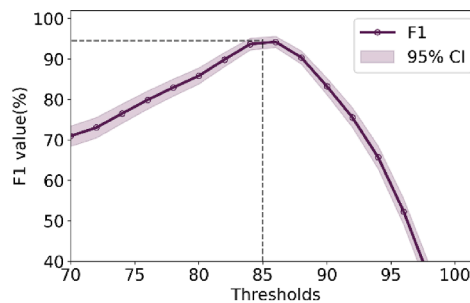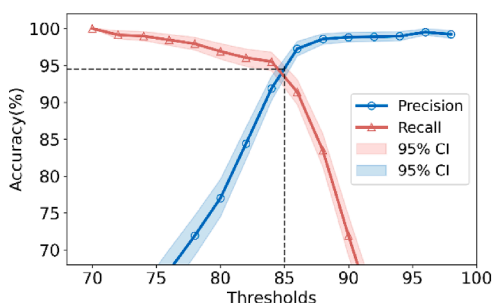
Fig. 3. Precision and recall curves under different thresholds. The shaded areas refer to 95% confidence interval.

4. Results and discussions

4.1. Validation and uncertainty estimates

A total of 6,370 sample points, including 688 wetland points and 5,682 non-wetland sampling points, are used to validate the accuracy of the wetland mapping. As listed in Table 1, the user's accuracy for wetland extraction is 95.5%, and the producer's accuracy is 90.1%. The F1 score for the wetland is 0.927, revealing a good balance between commission and omission errors. The high-quality extracted wetlands allow us to explore the spatio-temporal variations of the TP wetlands.

Standard Errors (SE) are presented in parentheses for the user's and producer's accuracy estimates.

The omission and commission error for mapping of the annual wetland maps arise from low-quality data (such as cloud cover), seasonal variations of wetlands, and other uncertainties related to model performance (Fuller et al., 2003; Murray et al., 2022; Xu, 2006). In this study, we used the images with<6% cloud cover. Clouds and cloud shadows cause uncertainty of wetland extraction. The cloud cover can account for the 6% of omission errors, but does not increase the commission error of wetland identification.

Another source of uncertainty comes from the seasonal dynamics of wetlands. Landsat imagery is the suitable data for mapping the long-term wetland changes in the TP due to its high spatial resolution (30 m) and long-term spans (Han et al., 2015). We use Landsat images during 1990–2019 in the same season as much as possible to identify wetlands. There is at least one scene covering every region from September to October, except for 1990, 1993, 1995, and 1999, and the images from other months are only used to replace those with cloud cover from September to October. This ensures the used images have the similar phenological and hydrological conditions as much as possible per year. Since the change of the wetlands within two consecutive months (from September to October) may be small, two or three scenes selected from September to October can capture the change of the wetland areal extent in a year to some degree. In addition, we focus on the wetland changes from 1990 to 2019 in this study, which further mitigates the uncertainty of the change caused by less image data in August-October.

The uncertainty estimates of the wetland areal extent are quantified by the confidence interval (CI). We use the standard error of the error-adjusted estimated areas with approximate 95% CI to estimate the upper and lower bounds of the areal extent of the extracted wetlands. The wetland areal extents in the TP are $154,454 \pm 7,813$ km^2 in 2019

and $202,611 \pm 10,249$ km^2 in 2019.

4.2. Spatial distribution of TP wetlands

Fig. 4 shows the number of years in which each location is identified to be occupied by wetland. Large spatial variations of wetlands exist on the TP. There are more wetlands on the northwest than the southeast of the TP, which are separated by the Xining-Xigaze line (red dashed line in Fig. 4). Overall, there are $167,713 \pm 8484$ km^2 of wetlands over the TP averaged over the 30 years, and its 30-year average wetland area fraction (ratio of the wetland area to the total area of the TP) reaches 6.4 %.

Considering the spatial heterogeneity of TP wetlands, we divide the TP into nine zones (Fig. 4) according to major rivers and watersheds provided by HydroSHEDS data sets(Lin et al., 2019; Xufeng, 2020; Zou et al., 2017), and explore the variability of wetlands across these zones. In the Yangtze River Basin (Zone 2), 63.6% of the wetlands are located in the west region of the Yangtze River (Zone 2w) averaged over the 30 years. Zone 2w is dominated by shallow valley landform with gentle slope and is different from the rest of Yangtze River Basin (Zone 2e) in terms of topography, geomorphology and wetland area fraction.
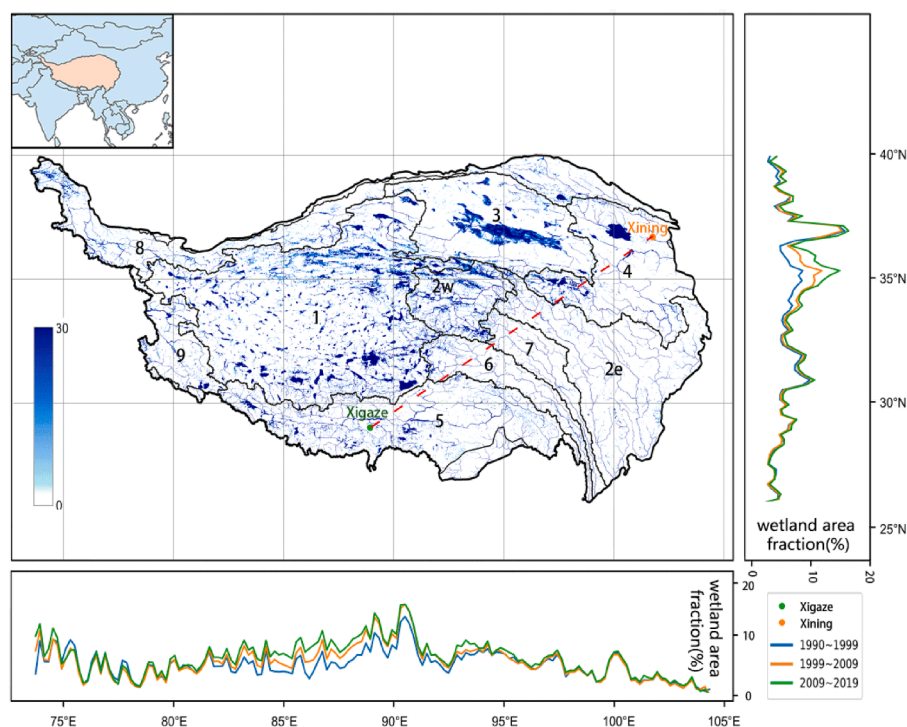
Qiangtang Plateau (Zone 1, mainly located at elevations of 4,400–5,200 m, Fig. 5), the western region of Yangtze River (Zone 2w, mainly located at 4,400–5,200 m and in the source region of Yangtze River) and Qaidam Basin (Zone 3 in Fig. 4, mainly located at 2,600–2,800 m) have about 61.3% of wetlands on the TP. They contain densely distributed wetlands and are dominated by lake and marsh wetlands. The average 30-year wetland areal extent on Qiangtang Plateau is the largest ($67,722 \pm 3426$ km^2), contributing 40.3 ± 2.0 % of the total wetland area on the TP. The wetland areal extent in the western region of Yangtze River contributes 8.4 ± 0.4 % ($14,124 \pm 714$ km^2) of TP wetlands. The Qaidam Basin (Zone 3) contributes 12.6 ± 0.6 % (21244 ± 1075 km^2) of the TP wetland area.

About 20.0% of the TP wetland area is located on the Yellow River Basin (Zone 4 in Fig. 4) and the Brahmaputra River Basin (Zone 5) where wetlands are distributed sparsely. The other wetlands (18.7%) are in the Salween River Basin (Zone 6), Mekong River Basin (Zone 7) and Yangtze River Basin outside the source region (Zone 2e) with lower wetland area fractions.

4.3. Temporal changes in TP wetlands

Over the past 30 years, the TP wetlands have experienced a rapidly increase by 31.2 ± 6.6 %, reaching $202,612 \pm 10,249$ km^2 (7.76 ± 0.39 % of the TP areal extent) in 2019 (Fig. 6). However, the wetland change is not linear. The wetland area reaches a minimum level in 1994. The first period of wetland area growth (by 27.5%) occurs over 1997–2002. Then, the wetland area fluctuates between 160,000 km^2 and 185,000 km^2 until 2015. From 2015 to 2018, the wetland area growth ($50,725 \pm 2,566$ km^2) is equivalent to about one third in 1990. The maximum wetland area of $218,591 \pm 11,057$ km^2 occurs in 2018.

Fig. 7 illustrates the wetland areal extent and the surface water body areal extent in each region. We notice that the latter accounts for 11.9%

Table 1
The error matrix of the validation samples for wetland extraction.

| Classes | Reference | | Total | UA%(SE) | F1 score |
	Wetlands	Other			
Wetland	657	31	688	95.5(1.5)	0.927
Other	72	5610	5682	98.8(0. 3)	
Total	729	5641	6370		
PA%(SE)	90.1(2.2)	99.5(0.2)			

Fig. 4. Distribution of TP wetlands. The map shows the number of years with wetlands in each location at a 30 m resolution from 1990 to 2019. On the sides are meridional (right panel) and zonal (bottom panel) distributions of 10-year average wetland area fraction over 1990–1999, 2000–2009 and 2010–2019 at a resolution of 0.02°. A total of nine zones is presented based on the division of watersheds, including 1: Qiangtang Plateau, 2: Yangtze River Basin, 3: Qaidam Basin, 4: Yellow River Basin, 5: Brahmaputra River Basin, 6: Salween River Basin, 7: Mekong River Basin, 8: Tarim Basin, and 9: Indus River Basin. Zone 2 is further separated into the western region of Yangtze River (2w) and the eastern region (2e). The orange and green dots represent Xining and Xigaze cities. (For interpretation of the references to colour in this figure legend, the reader is referred to the web version of this article.)
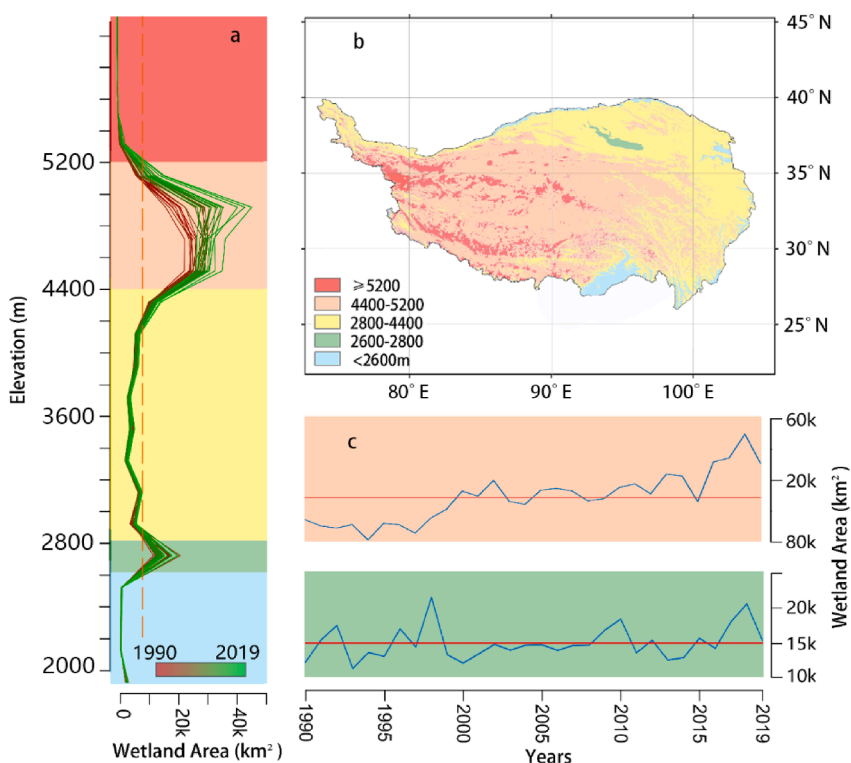

Fig. 5. Wetland distributions along altitude. a, Grouping and counting wetland areas at different altitudes at 200 m intervals. A total of 30 solid lines with different colors denote to the wetland distributions in each year between 1990 and 2019. The red broken line denotes the average wetland area. b, the elevation map of TP, where different elevation ranges are colored corresponding to the colors in a and c. c, the blue lines in the upper and lower charts show the changes of wetland area at 4400–5022 m and 2600–2800 m elevation ranges, respectively. (For interpretation of the references to colour in this figure legend, the reader is referred to the web version of this article.)

− 48.7% of the total wetland areas in the TP. The surface water body areal extent in Qiangtang Plateau (Zone 1) are the largest, accounting for 48.7% of the wetland areas, and that in Mekong River Basin (Zone 7) is the smallest, accounting for 11.9%. The surface water bodies in each zone showed an overall increase from 2000 to 2018. From 2000 to 2019, the growth rate of the wetlands in the TP was 17.3%, higher than that of surface water bodies (9.0%) except Mekong River Basin and Salween

River Basin. The wetland areal extent in Mekong River Basin (Zone 7) had a slight decline of 11.8 % from 1990 to 2019, and that in Salween River Basin (Zone 6) increased twice, i.e. from 4,445 ± 225 km2 to 4,809 ± 243 km2 in 1990–2004, and from 4,189 ± 212 km2 to 4,913 ± 249 km2 in 2005–2019. We also note that wetlands in the Yellow River Basin showed a downward trend before 1997, from 17,500 ± 885 km2 to 13,772 ± 697 km2, but gradually increased afterward. There was a
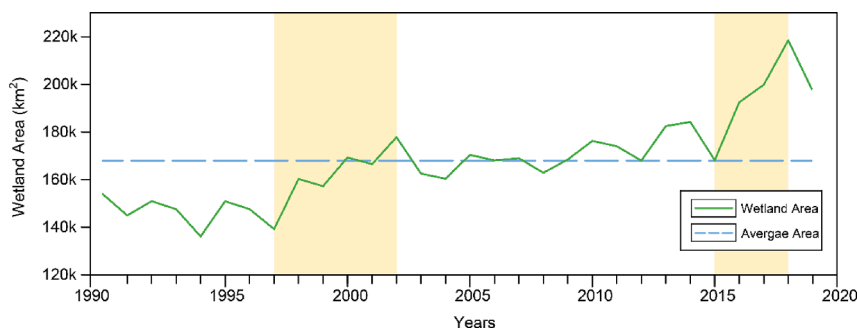
Fig. 6. Changes in TP wetland area from 1990 to 2019. The green curve represents the TP wetland area from 1990 to 2019, the broken blue line denotes the 30-year average, and the yellow shades represent two periods of significant growth. (For interpretation of the references to colour in this figure legend, the reader is referred to the web version of this article.)
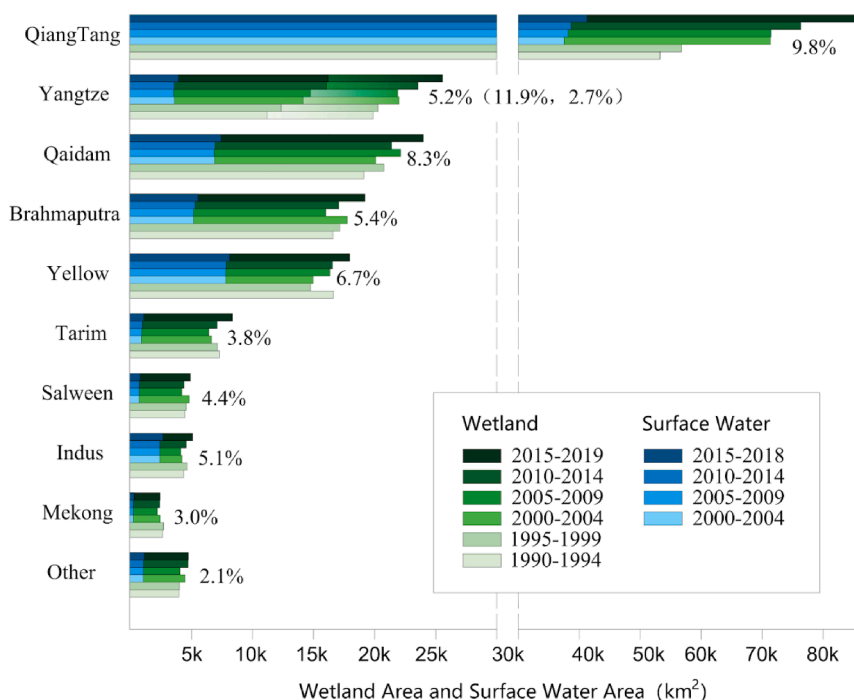
Fig. 7. Changes of wetlands in each region of TP. Take the average of every 5 years to calculate the wetland areal extent including surface water body areas in each region (the average of four years in 2015–2018). The changes have been made to the axis due to the prominent wetland and surface water area of Qiangtang Plateau. Percentage denotes the average wetland density of each region in 30 years. Left and right part of the group Yangtze bars in the histogram is for the source region of the Yangtze River and Yangtze River Basin region outside the source region, respectively. The wetland densities in the two regions in brackets of the Yangtze River also correspond to these two regions.

steady increase in Brahmaputra River Basin after 2009.

4.4. Impacts of climate variations on wetlands

Wetlands on the TP are highly sensitive to climate variability, albeit with limited influences by direct human disturbance (Arneth et al., 2010). We explore the associations between interannual wetland area changes and those in AT, AP and APE. Over the past 30 years, the AT has increased by 1.2 °C on the TP. The AP also has an increasing trend, but with much larger interannual fluctuations than AT. For example, AP shows substantial drops in 1994 and 2015 (from their previous years) due to drought.

Fig. 8b shows that the interannual changes in AT are significantly correlated with those in wetland areal extent at many places of the TP (p < 0.05 for 42.2% of area, and r > 0.8 for 11.5% of area). There are highly positive correlations over the majority of the northwest TP and weak or negative correlations on the southeast TP. The correlation between APE and wetland areal extent shows a similar spatial distribution (Fig. 8d). The correlation between AP and wetland area is statistically significant (p < 0.05) in 16.4% of area, which mainly exists on the Qiangtang Plateau and the Qaidam Basin. Considering the change of wetland areas was influenced by multiple climate factors, we used the

multiple linear regression model (MLM) to fit the relationship between the three factors and wetland areas. The estimated R^2 were 0.875, 0.867, 0.818 for Qiangtang Plateau, Yangtze River Source Region and Qaidam, respectively, meaning that the climate factors can explain 87.5%, 86.7% and 81.8% of the wetland area change on the three regions. Overall, the changes in wetland areal extent are highly positively correlated with the three climate parameters over the northwest TP, which includes Qiangtang Plateau, the source region of Yangtze River and Qaidam Basin.

The source region of the Yangtze River and Qiangtang Plateau are both concentrated areas of permafrost (Zou et al., 2017) (Fig. 9) due to their high altitudes (4,400–5,200 m). The warming induced permafrost melting creates many thaw lakes and exerts a strong control on wetland hydrology (Ran et al., 2018; Woo and Winter, 1993). Thaw lakes account for 71% of lakes on the above two zones in 2018, according to data from the National Cryosphere Desert Data Center (Chen et al., 2021). Thus, we examine the influence of permafrost thaw on the prevalence of wetlands by analyzing the change in the number of lakes. For Qiangtang Plateau and the source region of Yangtze River, we extract the lakes with area > 5,000 m² from the Landsat imagery in five periods including 1990-1991, 1996-1997, 2002, 2015 and 2018. Here, 1990-1991 is the starting time in our dataset, and the next four periods
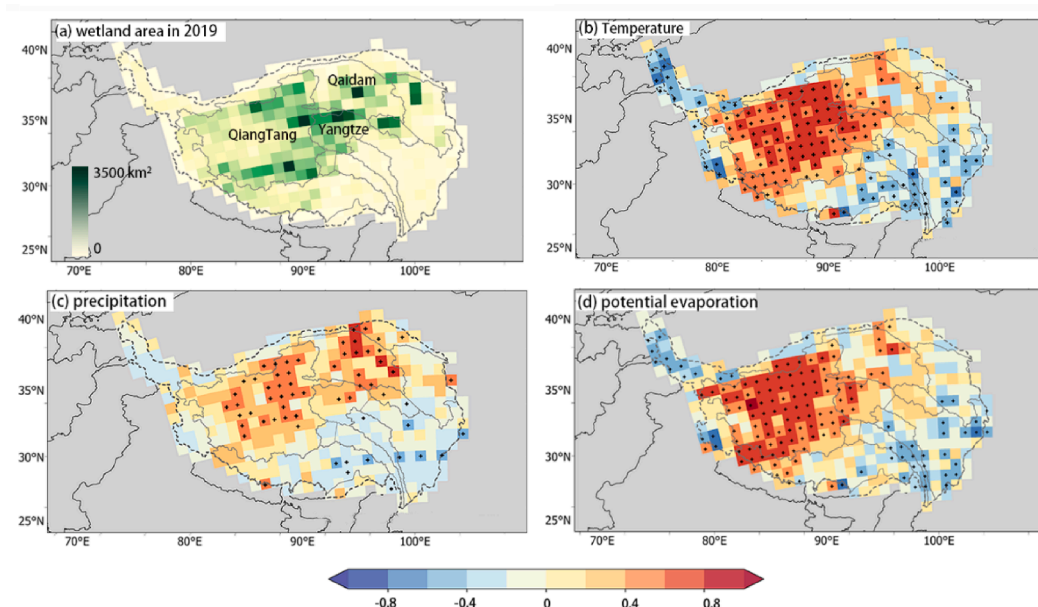
Fig. 8. Linking the wetland area variability to climate factors. Presented is the wetland area distribution in 2019 (a), as well as the correlations in interannual variability between wetland area and three meteoroidal parameters (b, c, d) at a resolution of approximately 90 km × 90 km. In b-d, the black dots denote statistically significant correlation (p < 0.05).
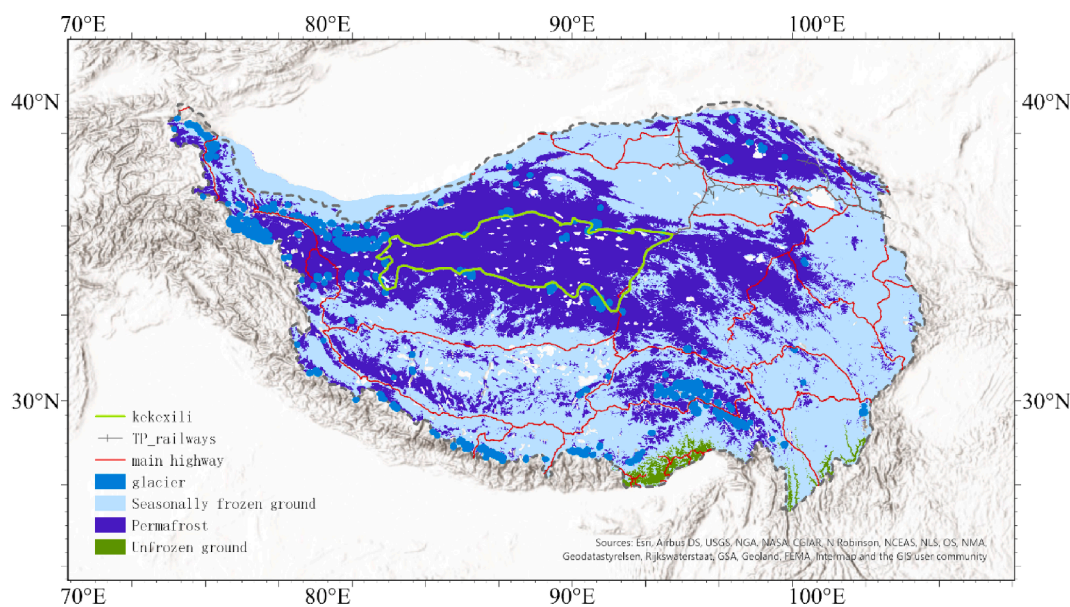
Fig. 9. Spatial distribution of permafrost on TP. The green line denotes the border of Hoh Xil. (For interpretation of the references to colour in this figure legend, the reader is referred to the web version of this article.)

are the beginning or end years of two major changes in wetland areal extent. During 1990–2018, the number of lakes has increased from 8,783 to 20,353, consistent with the increase in wetland area (Fig. 10). Therefore, the rising temperature may have resulted in permafrost thaw, which in turn have served as a dominant driver for wetland area growth in the source region of Yangtze River and Qiangtang Plateau.

In contrast, Qaidam Basin (Zone 3) contains little permafrost. In this zone, the river network is underdeveloped and runoff mainly comes from precipitation (Yang and Zhang, 1996). Among the three climatic factors, AP has the highest correlation with the wetland area (r = 0.685, P < 0.001).

The wetland areal extent in Yellow River Basin (Zone 4) exhibits a rapid decline by 21.3% from 1990 to 1997 and a steady growth

afterwards (Fig. 7). This trend has relatively low correlations with AT, AP and APE (r < 0.6). The wetland degradation in this zone before 1997 may be caused by human overgrazing, river siltation and soil erosion, and its growth after 1997 may be a combined result of regulation, ecological protection projects in the upper Yellow River and climate change (Jiang et al., 2013; Weixiao et al., 2019; Zhang et al., 2019).

The Brahmaputra River Basin (Zone 5) is located between the Kailas Range and Himalayas. The wetland area changes in this zone from 1990 to 2016 is more consistent with the trend of Brahmaputra runoff rather than climate variation. Wetlands of the Yangtze River Basin outside the source region (Zone 2e), Mekong Basin (Zone 7) and Salween Basin (Zone 6) are mainly river wetlands. Their landscapes are dominated by high mountain-gorge, with large depth of river valley undercutting, thus
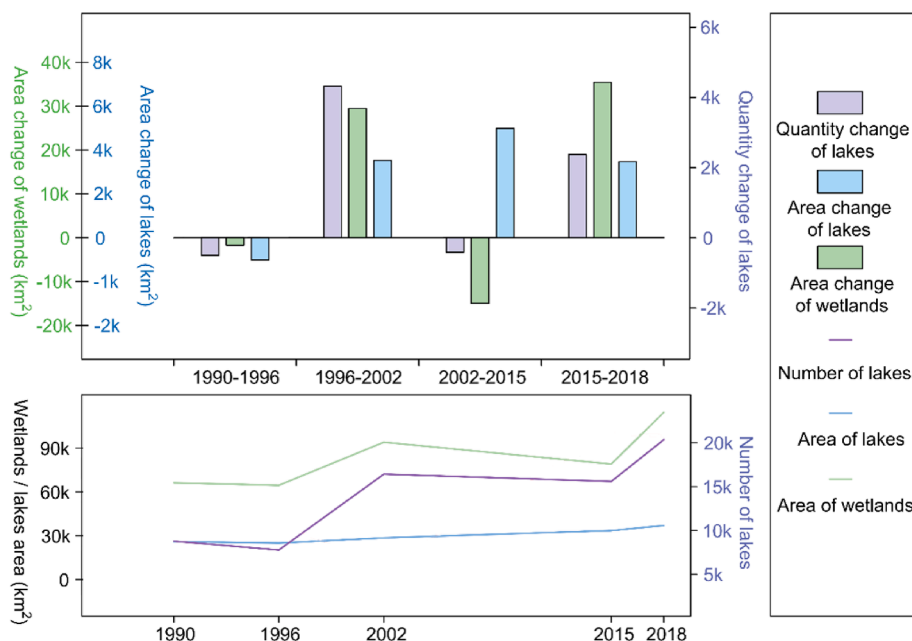
Fig. 10. Linking wetland area change to lakes. Changes in wetland areal extent, lake areal extent and lake number on the source region of the Yangtze River and Qiangtang Plateau.

water recharge and discharge are not easily reflected by wetland area.

5. Conclusion

Our study presents a new approach to quantify the long-term changes on the TP wetlands driven by climate variability. The contributions of this study can be summarized as follows: First, we propose a wetland extraction method based on the deep learning scene classification. By using the transfer learning training strategy, we achieve high wetland extraction accuracy with limited training samples. Second, we produce, for the first time, annual wetland maps covering the period from 1990 to 2019 in the TP, and analyze the spatiotemporal characteristics of wetland changes over the past 30 years. Third, we identify the impact of climate change on wetland area. The rapid wetland expansion is associated with increasing rainfall and rising temperature.

We find that over the past 30 years, the TP wetland area has increased substantially. The wetland growth might have changed the ecohydrological structure and affected plant growth, species composition and reproduction of various wildlife species. Moreover, the wetland expansion could result in gradual but prolonged release of greenhouse gases (Creed et al., 2017). As a sensitive region to climate change, the TP has been warming at twice the global warming rate (Medhaug et al., 2017). Recent decades have witnessed the most remarkable warming and permafrost thaw on the TP (Lei et al., 2021). Permafrost thaw triggered by rising temperature is linked to increase in wetland area in the source region of Yangtze River and Qiangtang Plateau from 1990 to 2019. The expansion in wetland areal extent is relatively small in 2000–2015, likely because of weaker global warming during this period (i.e., the hiatus (Medhaug et al., 2017)). The wetland area growth is rapid after 2015 (by 20.7% or 34,745 km²) in these two zones, consistent with the rapid global warming (Lei et al., 2021). According to the simulation of near-surface soil moisture evolution on permafrost regions (Avis et al., 2011), if warming continues, the permafrost surface will deepen and the near-surface moisture will drain to deeper soil layers, thus the wetlands may experience a sudden and rapid decline after continuous growth in these two zones.

There are some limitations in this study. We have only extracted the main wetland types like rivers, lakes and marshes. We do not explore the contribution of glacier melting to wetland expansion due to lack of

glacier data on the TP. In addition, the wetlands on Mekong River Basin have been shrinking, but the causes are still unclear.

Declaration of Competing Interest

The authors declare that they have no known competing financial interests or personal relationships that could have appeared to influence the work reported in this paper.

Data availability

Data will be made available on request.

References

Arneth, A., Harrison, S.P., Zaehle, S., Tsigaridis, K., Menon, S., Bartlein, P., Feichter, J., Korhola, A., Kulmala, M., O'donnell, D., others,, 2010. Terrestrial biogeochemical feedbacks in the climate system. Nat. Geosci. 3, 525–532.

Avis, C.A., Weaver, A.J., Meissner, K.J., 2011. Reduction in areal extent of high-latitude wetlands in response to permafrost thaw. Nat. Geosci. 4, 444–448.

Ayush, K., Uzkent, B., Meng, C., Tanmay, K., Burke, M., Lobell, D., Ermon, S., 2021. Geography-Aware Self-Supervised Learning. In: 2021 IEEE/CVF International Conference on Computer Vision (ICCV). IEEE, Montreal, QC, Canada, pp. 10161–10170.

Bargiel, D., 2017. A new method for crop classification combining time series of radar images and crop phenology information. Remote Sens. Environ. 198, 369–383.

Chatterjee, K., Bandyopadhyay, A., Ghosh, A., Kar, S., 2015. Assessment of environmental factors causing wetland degradation, using Fuzzy Analytic Network Process: A case study on Keoladeo National Park, India. Ecol. Model. 316, 1–13.

Xu Chen, Cuicui Mu, Lin Jia, Zhilong Li, Chengyan Fan, Mei Mu, Xiaoqing Peng, Xiaodong Wu, 2021. Thermokarst lakes on the Qinghai-Tibet Plateau (2018). National Tibetan Plateau Data Center.

Chen, J., Zhu, X., Vogelmann, J.E., Gao, F., Jin, S., 2011. A simple and effective method for filling gaps in Landsat ETM+ SLC-off images. Remote Sensing of Environment 115, 1053–1064.

Chmura, G.L., Anisfeld, S.C., Cahoon, D.R., Lynch, J.C., 2003. Global carbon sequestration in tidal, saline wetland soils. Global Biogeochem. Cycles 17.

Cohen, J., Agel, L., Barlow, M., Garfinkel, C.I., White, I., 2021. Linking Arctic variability and change with extreme winter weather in the United States. Science.

Creed, I.F., Lane, C.R., Serran, J.N., Alexander, L.C., Basu, N.B., Calhoun, A.J., Christensen, J.R., Cohen, M.J., Craft, C., D'Amico, E., et al., 2017. Enhancing protection for vulnerable waters. Nat. Geosci. 10, 809–815.

Davidson, N.C., 2014. How much wetland has the world lost? Long-term and recent trends in global wetland area. Mar. Freshw. Res. 65, 934–941.

Erwin, K.L., 2008. Wetlands and global climate change: the role of wetland restoration in a changing world. Wetlands Ecol Manage 17, 71.

Feng, S., Liu, S., Huang, Z., Jing, L., Zhao, M., Peng, X., Yan, W., Wu, Y., Lv, Y., Smith, A. R., et al., 2019. Inland water bodies in China: Features discovered in the long-term satellite data. Proc. Natl. Acad. Sci. 116, 25491–25496.

Fuller, R.M., Smith, G.M., Devereux, B.J., 2003. The characterisation and measurement of land cover change through remote sensing: problems in operational applications? Int. J. Appl. Earth Obs. Geoinf. 4, 243–253.

Gall, H.E., Park, J., Harman, C.J., Jawitz, J.W., Rao, P.S.C., 2013. Landscape filtering of hydrologic and biogeochemical responses in managed catchments. Landsc. Ecol. 28, 651–664.

Gong, P., Niu, Z.G., Cheng, X., Zhao, K.Y., Zhou, D.M., Guo, J.H., Liang, L., Wang, X.F., Li, D.D., Huang, H.B., Wang, Y., Wang, K., Li, W.N., Wang, X.W., Ying, Q., Yang, Z.Z., Ye, Y.F., Li, Z., Zhuang, D.F., Chi, Y.B., Zhou, H.Z., Yan, J., 2010. China's wetland change (1990–2000) determined by remote sensing. Sci. China Earth Sci. 53, 1036–1042.

Guo, M., Li, J., Sheng, C., Xu, J., Wu, L., 2017. A Review of Wetland Remote Sensing. Sensors 17, 777.

Han, X., Chen, X., Feng, L., 2015. Four decades of winter wetland changes in Poyang Lake based on Landsat observations between 1973 and 2013. Remote Sens. Environ. 156, 426–437.

Hogg, A., Todd, K.W., 2007. Automated discrimination of upland and wetland using terrain derivatives. Can. J. Remote. Sens. 33, S68–S83.

Hu, S., Niu, Z., Chen, Y., Li, L., Zhang, H., 2017. Global wetlands: Potential distribution, wetland loss, and status. Sci. Total Environ. 586, 319–327.

Hu, B., Shen, L., Lian, X., Zhu, Q., Liu, S., Huang, Q., He, Z., Geng, S., Cheng, D., Lou, L., et al., 2014. Evidence for nitrite-dependent anaerobic methane oxidation as a previously overlooked microbial methane sink in wetlands. Proc. Natl. Acad. Sci. 111, 4495–4500.

Hu, J., Shen, L., Sun, G., 2018. Squeeze-and-Excitation Networks. Proceedings of the IEEE Computer Society Conference on Computer Vision and Pattern Recognition 7132–7141.

Huang, C., Peng, Y., Lang, M., Yeo, I.Y., McCarty, G., 2014. Wetland inundation mapping and change monitoring using Landsat and airborne LiDAR data. Remote Sens. Environ. 141, 231–242.

Jiang, Ye, Sun, Jianguo, Xie, Jiali, 2013. Remote Sensing Assessment of Water and Soil Loss Changes of Zoige Wetland in Last 20 Years. Remote Sensing Technology and Application 28 (6), 1088–1093.

Kaiser, P., Wegner, J.D., Lucchi, A., Jaggi, M., Hofmann, T., Schindler, K., 2017. Learning Aerial Image Segmentation From Online Maps. IEEE Trans. Geosci. Remote Sensing 55, 6054–6068.

Kemker, R., Salvaggio, C., Kanan, C., 2018. Algorithms for semantic segmentation of multispectral remote sensing imagery using deep learning. ISPRS Journal of Photogrammetry and Remote Sensing, Deep Learning RS Data 145, 60–77.

Lei, J., Guo, X., Zeng, Y., Zhou, J., Gao, Q., Yang, Y., 2021. Temporal changes in global soil respiration since 1987. Nat. Commun. 12, 1–9.

Lin, Z., Guojie, H., Defu, Z., Xiaodong, W., Lu, M., Zhe, S., Liming, Y., Huayun, Z., Shibo, L., 2019. Permafrost changes and its effects on hydrological processes on Qinghai-Tibet Plateau. Bulletin of Chinese Academy of Sciences (Chinese Version) 34, 1233–1246.

Mañas, O., Lacoste, A., Giró-i-Nieto, X., Vazquez, D., Rodríguez, P., 2021. Seasonal Contrast: Unsupervised Pre-Training from Uncurated Remote Sensing Data. In: In: 2021 IEEE/CVF International Conference on Computer Vision (ICCV). Presented at the 2021 IEEE/CVF International Conference on Computer Vision (ICCV), pp. 9394–9403.

Mao, D., Wang, Z., Du, B., Li, L., Tian, Y., Jia, M., Zeng, Y., Song, K., Jiang, M., Wang, Y., 2020. National wetland mapping in China: A new product resulting from object-based and hierarchical classification of Landsat 8 OLI images. ISPRS J. Photogramm. Remote Sens. 164, 11–25.

Martens, B., Miralles, D.G., Lievens, H., Van Der Schalie, R., De Jeu, R.A., Fernández-Prieto, D., Beck, H.E., Dorigo, W.A., Verhoest, N.E., 2017. GLEAM v3: Satellite-based land evaporation and root-zone soil moisture. Geoscientific Model Development 10, 1903–1925.

Medhaug, I., Stolpe, M.B., Fischer, E.M., Knutti, R., 2017. Reconciling controversies about the 'global warming hiatus'. Nature 545, 41–47.

Mitsch, W.J., Bernal, B., Nahlik, A.M., Mander, Ü., Zhang, L., Anderson, C.J., Jørgensen, S.E., Brix, H., 2013. Wetlands, carbon, and climate change. Landscape Ecol 28, 583–597.

Murray, N.J., Worthington, T.A., Bunting, P., Duce, S., Hagger, V., Lovelock, C.E., Lucas, R., Saunders, M.I., Sheaves, M., Spalding, M., Waltham, N.J., Lyons, M.B., 2022. High-resolution mapping of losses and gains of Earth's tidal wetlands. Science 376, 744–749.

Niu, Z.G., Zhang, H.Y., Wang, X.W., Yao, W.B., Zhou, D.M., Zhao, K.Y., Zhao, H., Li, N.N., Huang, H.B., Li, C.C., Yang, J., Liu, C.X., Liu, S., Wang, L., Li, Z., Yang, Z.Z., Qiao, F., Zheng, Y.M., Chen, Y.L., Sheng, Y.W., Gao, X.H., Zhu, W.H., Wang, W.Q., Wang, H., Weng, Y.L., Zhuang, D.F., Liu, J.Y., Luo, Z.C., Cheng, X., Guo, Z.Q., Gong, P., 2012. Mapping wetland changes in China between 1978 and 2008. Chin. Sci. Bull. 57, 2813–2823.

Pekel, J.F., Cottam, A., Gorelick, N., Belward, A.S., 2016. High-resolution mapping of global surface water and its long-term changes. Nature 540, 418–422.

Ran, Y., Li, X., Cheng, G., 2018. Climate warming over the past half century has led to thermal degradation of permafrost on the Qinghai-Tibet Plateau. Cryosphere 12, 595–608.

Stehman, S.V., Foody, G.M., 2019. Key issues in rigorous accuracy assessment of land cover products. Remote Sens. Environ. 231, 111199.

Russi, D., ten Brink, P., Farmer, A., Badura, T., Coates, D., Förster, J., Kumar, R., Davidson, N., 2013. The economics of ecosystems and biodiversity for water and wetlands. IEEP, London and Brussels 78, 118p.

Sun, C., Shrivastava, A., Singh, S., Gupta, A., 2017. Revisiting unreasonable effectiveness of data in deep learning era. In: Proceedings of the IEEE International Conference on Computer Vision. pp. 843–852.

Tian, H., Lu, C., Ciais, P., Michalak, A.M., Canadell, J.G., Saikawa, E., Huntzinger, D.N., Gurney, K.R., Sitch, S., Zhang, B., et al., 2016. The terrestrial biosphere as a net source of greenhouse gases to the atmosphere. Nature 531, 225–228.

Wang, B., Ma, Y., Su, Z., Wang, Y., Ma, W., 2020a. Quantifying the evaporation amounts of 75 high-elevation large dimictic lakes on the Tibetan Plateau. Science advances 6 (26), eaay8558.

Wang, X., Xiao, X., Zou, Z., Dong, J., Qin, Y., Doughty, R.B., Menarguez, M.A., Chen, B., Wang, J., Ye, H., Ma, J., Zhong, Q., Zhao, B., Li, B., 2020b. Gainers and losers of surface and terrestrial water resources in China during 1989–2016. Nat. Commun. 11, 1–12.

Wang, Y., Zhang, L., Mathiopoulos, P.T., Deng, H., 2015. A Gestalt rules and graph-cut-based simplification framework for urban building models. Int. J. Appl. Earth Obs. Geoinf. 35, 247–258.

Wei, P., Chai, D., Huang, R., Peng, D., Lin, T., Sha, J., Sun, W., Huang, J., 2022. Rice mapping based on Sentinel-1 images using the coupling of prior knowledge and deep semantic segmentation network: A case study in Northeast China from 2019 to 2021. Int. J. Appl. Earth Obs. Geoinf. 112, 102948.

Weixiao, H., Chunlin, H., Yunchen, W., Juan, G., 2019. Study on the Area Variation of Qinghai Lake Based on Long-Term Landsat 5/8 Multi-Band Remote Sensing Imagery. Advances in Earth Science 34, 346–355.

Woo, M.-K., Winter, T.C., 1993. The role of permafrost and seasonal frost in the hydrology of northern wetlands in North America. J. Hydrol. 141, 5–31.

Xi, Y., Peng, S., Ciais, P., Chen, Y., 2020. Future impacts of climate change on inland Ramsar wetlands. Nature Climate Change.

Xu, H., 2006. Modification of normalised difference water index (NDWI) to enhance open water features in remotely sensed imagery. Int. J. Remote Sens. 27, 3025–3033.

Xufeng, W., 2020. The Boundary Dataset of The Three-River-Source National Park. National Tibetan Plateau Data Center.

Yang, G.L., Zhang, J.X., 1996. Hydrological characteristics of Qaidam Basin. Arid Zone Res. 13, 7–13.

Zhang, Z., Zimmermann, N.E., Stenke, A., Li, X., Hodson, E.L., Zhu, G., Huang, C., Poulter, B., 2017. Emerging role of wetland methane emissions in driving 21st century climate change. Proceedings of the National Academy of Sciences 114, 9647–9652.

Zhang, J., Liu, J., Jin, L., Ma, T., Wang, G., Liu, H., Min, X., Wang, H., Lin, J., Bao, Z., others, 2019. Evolution and Trend of Water Resources in Qinghai-Tibet Plateau. Bull. Chin. Acad. Sci 34, 1264–1273.

Zhao, C., Zhang, Y., Liu, L., Liu, F., Zhang, H., 2015. Recent changes in wetlands on the Tibetan Plateau: a review. J. Geogr. Sci. 25, 879–896.

Zhou, Y., Dong, J., Xiao, X., Xiao, T., Yang, Z., Zhao, G., Zou, Z., Qin, Y., 2017. Open surface water mapping algorithms: a comparison of water-related spectral indices and sensors. Water 9, 256.

Zou, D., Zhao, L., Sheng, Y., Chen, J., Hu, G., Wu, T., Wu, J., Xie, C., Wu, X., Pang, Q., Wang, W., Du, E., Li, W., Liu, G., Li, J., Qin, Y., Qiao, Y., Wang, Z., Shi, J., Cheng, G., 2017. A new map of permafrost distribution on the Tibetan Plateau. Cryosphere 11, 2527–2542.